

P²AD: Learning Point-wise Abstaining Penalty for Point Cloud Anomaly Detection

Shaocong Xu^{1,2}, Pengfei Li¹, Xinyu Liu¹, Qianpu Sun¹, Yang Li¹, Shihui Guo², Zhen Wang³, Bo Jiang³, Rui Wang³, Kehua Sheng³, Bo Zhang³, Hao Zhao¹

¹Tsinghua University, Beijing, China

²Xiamen University, Xiamen, China

³Didi Chuxing, Beijing, China

xushaocong@stu.xmu.edu.cn, {li-pf22,sqp23}@mails.tsinghua.edu.cn, liuxinyu@stu.xidian.edu.cn, {liyang,zhaohao}@air.tsinghua.edu.cn, guoshihui@xmu.edu.cn, {wangzhenwangzhen, scottjiangbo, raywangrui, shengkehua, zhangbo}@didiglobal.com

Abstract

LiDAR-based semantic scene understanding is an important module in the modern autonomous driving perception stack. However, identifying Out-Of-Distribution (OOD) points in a LiDAR point cloud is challenging as point clouds lack semantically rich features when compared with RGB images. We revisit this problem from the perspective of selective classification, which introduces a selective function into the standard closed-set classification setup. Our solution is built upon the basic idea of abstaining from choosing any known categories but learns a point-wise abstaining penalty with a margin-based loss. Synthesizing outliers to approximate unlimited OOD samples is also critical to this idea, so we propose a strong synthesis pipeline that generates outliers originated from various factors: unrealistic object categories, sampling patterns and sizes. We demonstrate that learning different abstaining penalties, apart from point-wise penalty, for different types of (synthesized) outliers can further improve the performance. We benchmark our method on SemanticKITTI and nuScenes and achieve state-of-the-art results. Risk-coverage analysis further reveals intrinsic properties of different methods. Codes and models will be publicly available.

Introduction

3D LiDAR sensors have been widely adopted in modern autonomous cars, primarily due to their capability to directly capture precise and long-range distance measurements of the surrounding environment, when compared with RGB cameras. However, LiDARs are not perfect and a notable disadvantage is the lack of semantically rich features. Human eyes can easily recognize semantic categories from an RGB image while the task becomes substantially more difficult when the input is a LiDAR point cloud. This conclusion also holds for machine eyes (i.e., computer vision algorithms), as evidenced by the fact that LiDAR-based semantic segmentation usually under-performs its RGB-based counterpart.

The lack of semantically rich features also negatively impacts LiDAR-based road anomaly detection. Road anomaly detection is an extension of semantic segmentation, which aims to identify regions not belonging to the pre-defined label set. RGB-based road anomaly detection draws a lot of attention recently from both academia and industry and sees remarkable progress (Tian et al. 2022; Liu et al. 2022; Tian

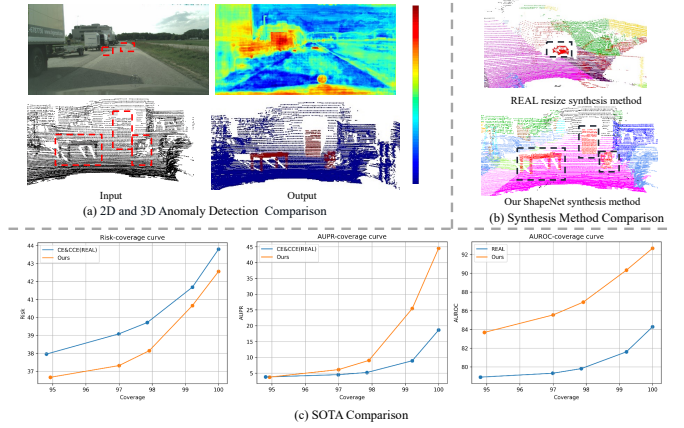


Figure 1: a. 3D anomaly detection is much more difficult than its 2D counterpart; b. Comparison of our ShapeNet-based synthesis pipeline and the former resizing-based synthesis pipeline; c. Comparison of our method with REAL in SemanticKITTI using Risk-Coverage, AUPR-Coverage, and AUROC-Coverage curves. Our method is better.

et al. 2023). By contrast, LiDAR-based anomaly detection (Cen et al. 2022) is still in a very early stage and reports poor quantitative results on public benchmarks. The focus of this study is to address this important yet challenging problem.

The aforementioned difficulty is demonstrated through Fig. 1-(a). As shown in the upper panel, although this is an extremely difficult case in which the anomaly is very small, we can still find the plank left on the road. Meanwhile, the SOTA algorithm successfully highlights it in the heatmap. On the contrary, detecting anomaly in a point cloud is much more challenging due to the lack of semantically rich features, shown in the lower panel of Fig. 1-(a). There is some furniture on the road, which is clearly anomalous, but both human eyes and computer vision algorithms struggle to identify them.

How to capture the subtle differences between known and anomalous classes in a LiDAR point cloud? We make contributions from both the perspective of **formulation** and **data**.

Formulation. REAL (Cen et al. 2022) exploits dummy classifiers to aggregate information in anomalous objects,

which is spiritually similar to Selective Classification (SC) (Feng et al. 2023). We reformulate the point cloud anomaly detection problem strictly using the principle of SC. What’s more, we learn the abstaining penalty in a point-wise manner, which can better capture the subtle difference in point clouds. Meanwhile, our formulation also learns different penalties for different data sources. Finally, we go back to the origin of SC and delve into the risk-coverage analysis. As illustrated in Fig. 1-(c), our method exhibits a significantly better performance compared to REAL across various levels of coverage, demonstrating its superiority. Through the lens of risk-coverage curve, we attain a deeper understanding of the performance gains achieved by our approach, and insights into the nature of different methods.

Data. The SOTA method (Cen et al. 2022) synthesizes pseudo anomalous objects by resizing known objects, as shown in the upper panel of Fig. 1-(b). However, we observe that pseudo anomalous objects synthesized in this way fail to well represent the long-tail distribution of road anomalies, in two regards. **Firstly**, objects from existing road scene understanding datasets are limited in category and thus resizing them hardly compensates for the lack of semantically rich features. **Secondly**, naive resizing violates the sampling pattern of real LiDAR sensors: points on enlarged objects get sparser while those on shrunk objects get denser. This leads to a shortcut problem: the model may find a trivial solution to distinguish pseudo anomalous objects from known objects solely using sparsity.

To generate better pseudo anomalous objects, we propose to introduce objects from an external dataset, ShapeNet (Chang et al. 2015), into existing scenes. Specifically, we merge randomly selected ShapeNet objects into road scenes by changing the radii of certain scene points in spherical coordinates. By replacing the radii, we preserve the sampling pattern of realistic point clouds as shown in the lower panel of Fig. 1-(b). We compensate for the lack of semantically rich features in point clouds by incorporating semantically rich anomalous objects, as ShapeNet covers a wide spectrum of categories.

Our contributions can be summarized as follows:

- We propose a new approach for endowing 3D segmentation models with the capability of detecting anomalies, which can be utilized in conjunction with existing segmentation models.
- We utilize ShapeNet object as a guide to modify the radii of existing points to synthesize more realistic and more diverse anomalies.
- We incorporate risk-coverage curve metrics into our evaluation process. By utilizing risk-coverage curve analysis, we are able to identify the nature of improvements and gain valuable insights into the strengths and weaknesses of different approaches.
- Our proposed method has achieved new SOTA performance for anomaly detection not only in previously established anomaly detection metrics, but also in the newly introduced risk-coverage curve metric, on SemanticKITTI and NuScenes.

Selective Classification Problem Formulation

The seminal point cloud anomaly detection method REAL (Cen et al. 2022) lacks a principled framework, hindering both theoretical and experimental analysis. So we first formalize the definition of SC and put different methods under a unified **theoretical** lens. **Experimentally**, the risk-coverage trade-off analysis that comes along with this framework, allows us to reveal in-depth differences between methods.

In SC, our goal is to learn predictive models that know what they do not know or when they should abstain¹ from making decisions. Here we consider a generic SC definition, which is agnostic of network and application. A supervised classification task is formulated as follows. Let \mathcal{X} be any feature space and \mathcal{Y} a label space. In point cloud anomaly detection, \mathcal{X} could be point clouds, and \mathcal{Y} could be class labels² of each point cloud. Let $P(\mathcal{X}, \mathcal{Y})$ be a distribution over $\mathcal{X} \times \mathcal{Y}$. A model $f : \mathcal{X} \rightarrow \mathcal{Y}$ is called a prediction function and its true risk used to evaluate the performance of f w.r.t. P is $R(f) := E_{P(\mathcal{X}, \mathcal{Y})}[\ell(f(\mathbf{x}), \mathbf{y})]$, where $\ell : \mathcal{Y} \times \mathcal{Y} \rightarrow \mathbb{R}^+$ is a given loss function, for example, the Cross Entropy (CE) loss. Given a labeled set $S_m = \{(\mathbf{x}_i, \mathbf{y}_i)\}_{i=1}^m \subseteq (\mathcal{X} \times \mathcal{Y})^m$ sampled i.i.d. from $P(\mathcal{X}, \mathcal{Y})$, the empirical risk of the classifier f is $\hat{r}(f|S_m) := \frac{1}{m} \sum_{i=1}^m \ell(f(\mathbf{x}_i), \mathbf{y}_i)$.

Apart from risk, another important concept in the SC formulation is coverage. A selective model (El-Yaniv et al. 2010) is a pair (f, g) , where f is a prediction function, and $g : \mathcal{X} \rightarrow \{0, 1\}$ is a selective function, which serves as a binary qualifier for f as follows:

$$(f, g)(\mathbf{x}) := \begin{cases} f(\mathbf{x}), & \text{if } g(\mathbf{x}) = 1 \\ \text{ABSTAIN}, & \text{if } g(\mathbf{x}) = 0 \end{cases} \quad (1)$$

Thus, the selective model abstains from prediction at \mathbf{x} iff $g(\mathbf{x}) = 0$. A soft selection function can also be considered, where $g : \mathcal{X} \rightarrow [0, 1]$, and decisions can be taken probabilistically or deterministically (e.g., using a threshold). The introduction of a selective function g allows us to define coverage. Specifically, coverage is defined to be the ratio of the non-abstained subset within set P to the entirety of P , which can be formulated as:

$$\phi(g) := E_P[g(\mathbf{x})] \quad (2)$$

Accordingly, the standard risk for a classifier f can be augmented into the selective risk of (f, g) as

$$R(f, g) := \frac{E_P[\ell(f(\mathbf{x}), \mathbf{y})g(\mathbf{x})]}{\phi(g)} \quad (3)$$

Clearly, the risk of a selective model can be traded-off for coverage. The performance profile of such a model can be specified by its risk-coverage curve, defined to be the risk as a function of coverage.

Remark. Later we will put different methods under the unified lens of SC and use the risk-coverage curve to probe their intrinsic properties.

Finally, we clarify that the continuous risk and coverage defined above are empirically calculated using a fixed set in practice. For any given labeled set S_m , the empirical selective risk is

$$\hat{r}(f, g|S_m) := \frac{\frac{1}{m} \sum_{i=1}^m \ell(f(\mathbf{x}_i), \mathbf{y}_i)g(\mathbf{x}_i)}{\phi(g|S_m)} \quad (4)$$

¹The abstaining penalty will be defined later.

²These class labels include an outlier label.

and the empirical coverage is

$$\hat{\phi}(g|S_m) := \frac{1}{m} \sum_i^m g(\mathbf{x}_i) \quad (5)$$

Related Works

Anomaly Detection in Autonomous Driving. Anomaly detection in autonomous driving is vital for ensuring the safety of ego-cars in open-world environments by identifying OOD objects. Extensive research has been conducted in 2D perception, specifically with semantic segmentation models. Unsupervised methods (Jung et al. 2021; Bevandić et al. 2021) involve post-processing predicted logits from frozen segmentation models to detect anomalies. Supervised methods (Tian et al. 2022; Grcić, Bevandić, and Šegvić 2022; Chan, Rottmann, and Gottschalk 2021) utilize auxiliary datasets like COCO (Lin et al. 2014) to synthesize anomaly objects in training images (e.g., Cityscapes (Cordts et al. 2016)) and retrain the segmentation model using outlier exposure (Hendrycks, Mazeika, and Dietterich 2018).

While significant advancements have been made in 2D anomaly detection, the exploration in the context of 3D point clouds remains limited. Cen et al. (2022) use resizing-based synthesis pipeline and calibration loss to achieve the discrimination of anomaly points. However, their focus primarily revolves around the open-world segmentation setting without extensively analyzing calibration effectiveness. Li and Dong (2023) propose an adversarial prototype framework that improves performance but involves complex network design and computationally expensive training. Considering these limitations, we present our method and substantiate its effectiveness through extensive experiments.

Selective Classification. SC can be broadly classified into two groups: 1) the first group focuses on addressing SC through the use of additional heads/logits (Geifman and El-Yaniv 2017, 2019; Liu et al. 2019; Feng et al. 2023; Gal and Ghahramani 2016; Chow 1970); 2) the second group tackles SC through cost-sensitive classification techniques (Charoenphakdee et al. 2021; Mozannar and Sontag 2020). Motivated by the extra head/logits design, resembling anomaly detection, we design new anomaly detector from the perspective of SC and utilize SC’s evaluation metrics as alternative performance measures for our anomaly detector.

Synthetic Data. Due to the limited availability and high cost associated with acquiring high-quality real-world datasets, synthetic data has been extensively employed in the field of scene understanding (Su et al. 2015; Movshovitz-Attias, Kanade, and Sheikh 2016; Zhang et al. 2017b; Handa et al. 2016; McCormac et al. 2017; Zhang et al. 2017a; Song et al. 2017). In this work, we introduce ShapeNet objects into the existing scene to effectively compensate for the lack of semantically rich features in point clouds.

Method

3D semantic segmentation is the task of assigning a class label to each point in a given LiDAR point cloud. Anomaly detection, on the other hand, is an extension to semantic segmentation, which aims to identify points that do not belong

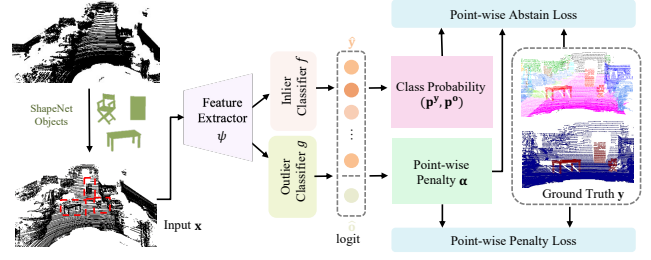


Figure 2: Our method’s pipeline: LiDAR point cloud input is processed by a feature extractor to extract features. These features are then used by the inlier and outlier classifiers to predict class logits. Point-wise abstain and penalty loss are calculated based on these predictions.

to the predefined inlier label set (learning to detect anomalous outliers). While the seminal work (Cen et al. 2022) proposes a viable solution REAL, we revisit it using the unified theoretical framework of SC and propose ours that effectively addresses the lack of semantically rich features.

Apart from the formulation contribution, we also make a contribution from the perspective of data. We design a novel anomaly synthesis pipeline that leverages the richness of the ShapeNet and adheres to the realistic LiDAR distribution to compensate for the lack of semantically rich features.

Architecture Overview

As shown in Fig. 2, the input LiDAR point cloud $\mathbf{x} \in \mathbb{R}^{n \times 3}$, sampled from S_m , is denoted on the left with ShapeNet objects integrated into it. Then, \mathbf{x} is fed into the feature extractor ψ followed by a inlier classifier f to predict the inlier logit $\hat{\mathbf{y}} \in \mathbb{R}^{n \times c}$, where c is the number of inlier classes. Additionally, an outlier classifier g is employed to predict the outlier logit $\hat{\mathbf{o}} \in \mathbb{R}^{n \times 1}$. As such, (f, g) instantiates a selective model mentioned above. These operations can be expressed as follows:

$$\begin{aligned} \hat{\mathbf{y}} &:= f(\psi(\mathbf{x})) \\ \hat{\mathbf{o}} &:= g(\psi(\mathbf{x})) \\ \tilde{\mathbf{y}} &:= [\hat{\mathbf{y}}, \hat{\mathbf{o}}] := \left\{ \tilde{\mathbf{y}}_i := [\hat{y}_i, \hat{o}_i] \mid i = 1, \dots, n \right\} \\ \mathbf{p} &:= \left\{ p_{i,j} = \frac{e^{\tilde{y}_{i,j}}}{\sum_{k=1}^{c+1} e^{\tilde{y}_{i,k}}} \mid i = 1, \dots, n; j = 1, \dots, c+1 \right\} \\ \mathbf{p}^y, \mathbf{p}^o &:= \mathbf{p} \end{aligned} \quad (6)$$

Here, the operation $[\cdot]$ denotes concatenation. Prediction probability $\mathbf{p} \in [0, 1]^{n \times (c+1)}$ consists of inlier probability $\mathbf{p}^y \in [0, 1]^{n \times c}$ and outlier probability $\mathbf{p}^o \in [0, 1]^{n \times 1}$.

Revisiting the REAL Formulation

Cen et al. (2022) introduce the first approach REAL to conduct anomaly detection in LiDAR point clouds. Their added dummy classifiers can also be thought of as g , under the SC framework, but there is a key difference. They observe

Table 1: Removing CCE in REAL can actually improve the anomaly detection metrics on SemanticKITTI.

CE	CCE	AUPR	AUROC	mIoU _{old}
✓	✓	20.00	84.90	57.80
✓		26.68	87.60	58.28

that numerous real outliers are wrongly classified as inlier classes with high probabilities. To address this issue, they propose a Calibration Cross Entropy (CCE) loss function to drive the outlier logit of the inlier sample to the second largest. We formalize³ this loss as follows:

$$\ell := \underbrace{\frac{1}{m} \sum_{S_m} \frac{1}{n} \sum_{i=1}^n \left\{ -\log \frac{e^{\tilde{y}_{i,y_i}}}{\sum_{k=1}^{c+1} e^{\tilde{y}_{i,k}}} \right\}}_{\text{CE}} - \underbrace{\lambda \mathbb{I}(y_i \neq c+1) \log \frac{e^{\tilde{y}_{i,c+1}}}{\sum_{k=1 \& k \neq y_i}^{c+1} e^{\tilde{y}_{i,k}}}}_{\text{CCE}} \quad (7)$$

Here, $y_i \in \{1, \dots, c, c+1\}$ signifies the ground truth corresponding to $x_i \in \mathbf{x}$, where $\{1, \dots, c\}$ represents inlier class labels while $\{c+1\}$ indicates the outlier class label. \mathbf{y} and \mathbf{x} are sampled i.i.d. from S_m . $\mathbb{I}(\cdot)$ is the indicator function. λ is a hyperparameter. A notable fact is that REAL does not provide an ablation study for this CCE loss and as shown in Tab. 1, removing this CCE loss can indeed significantly improve standard anomaly detection metrics. But why this happens cannot be understood through metrics like AUPR or AUROC, highlighting the need to revisit REAL under the lens of SC. Specifically, under the SC perspective, we can use the risk-coverage analysis to investigate it.

A Closer Look

We use Fig. 3 as an intuitive case to analyze the negative impact of the CCE loss. It illustrates sample numbers within different \mathbf{p}^o intervals for both inliers and outliers. By removing the CCE loss, sample number in the extremely low interval $[0, 0.1]$ grows significantly for both inliers and outliers. This is desirable for inliers but not for outliers. As shown by the red increase number, 9.8 million samples change to a desirable state while 1.7 million samples change to a undesirable state, and this large difference explains why the collective metrics in Tab. 1 become better.

The reason why this in-depth statistics (Fig. 3) can reveal the negative impact of CCE is that different \mathbf{p}^o values are investigated separately. And, the SC framework provides the principled tool risk-coverage curve to conduct this kind of analysis, because different coverage is achieved through selecting different thresholds on \mathbf{p}^o . More principled analyses that reveal reasons behind phenomena like Tab. 1 can be found in the experiments section.

³This is equivalent to the loss used in the REAL paper although REAL describes it in a different manner.

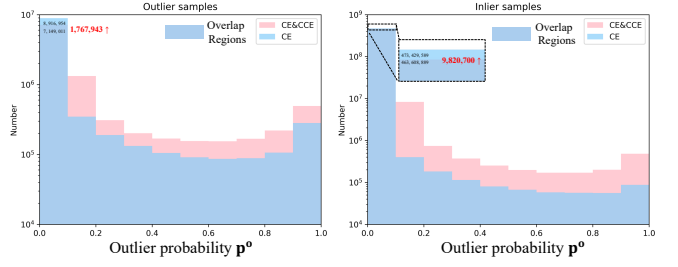


Figure 3: Statistics of outlier probability \mathbf{p}^o for inlier and outlier samples under different settings of REAL on SemanticKITTI. For inlier samples, we would like to observe more samples with $\mathbf{p}^o \in [0, 0.1]$, while for outlier samples, less samples with $\mathbf{p}^o \in [0, 0.1]$ is desirable.

Point-wise Abstaining Penalty Training Paradigm

Now that we have taken the perspective of SC, we argue that making the selective function g better is the key factor. Recall that our architecture (Fig. 2) directly predicts the outlier probability \mathbf{p}^o , on which we can impose different thresholds to achieve different coverage. Our proposal is to replace REAL’s problematic loss with a new one that imposes abstaining penalty on the outlier probability \mathbf{p}^o :

$$\ell^{\text{abstain}} := \underbrace{\frac{1}{m} \sum_{S_m} \frac{1}{n} \sum_{i=1}^n \left\{ -\mathbb{I}(y_i \neq c+1) \log \left\{ p_{i,y_i}^y + \underbrace{\frac{p_i^o}{(-\alpha_i)^2}}_{\text{abstaining term}} \right\} \right\}}_{\text{for inlier samples}} - \underbrace{\mathbb{I}(y_i = c+1) \sum_{j=1}^c \log \left\{ p_{i,j}^y + \underbrace{\frac{p_i^o}{(-\alpha_i)^2}}_{\text{abstaining term}} \right\}}_{\text{for outlier samples}} \quad (8)$$

The α value denotes the point-wise penalty that controls the tendency to abstain or not. Since this value is defined in a point-wise manner, it has the potential to capture the subtle difference between inliers and outliers despite point clouds lack semantically rich features for anomaly detection. Collaborating with the above **point-wise abstain loss** (right-top in Fig. 2), we introduce a **point-wise penalty loss** (right-

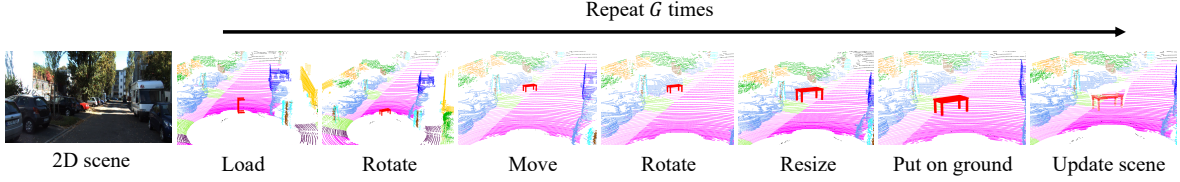


Figure 4: Anomaly synthesis pipeline.

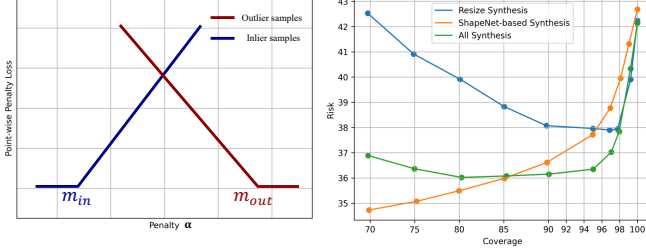


Figure 5: Left: Relationship between point-wise penalty loss and penalty α . Right: Comparison with different anomaly synthesis pipeline using the risk-coverage curve.

bottom in Fig. 2), which is expressed as follows:

$$\alpha := \left\{ \alpha_i = -\log\left(\sum_{j=1}^c e^{\hat{y}_{i,j}}\right) \mid i = 1, \dots, n \right\}$$

$$\ell^{\text{penalty}} := \frac{1}{m} \sum_{S_m} \frac{1}{n} \sum_{i=1}^n \left\{ \mathbb{I}(y_i \neq c+1) \max(\alpha_i - m_{in}, 0) \right. \\ \left. + \mathbb{I}(y_i = c+1) \max(m_{out} - \alpha_i, 0) \right\} \quad (9)$$

As shown in Fig. 5-left, the hyperparameters m_{in} and m_{out} ensure that the inlier samples are associated with penalties lower than m_{in} , while the outlier samples exhibit penalties higher than m_{out} . Note that in our experiments, the penalties are negative as we set the value of m_{in} to -12, and m_{out} to -6. Intuitively, minimizing the point-wise penalty loss assigns lower α_i penalties to inlier samples. This results in higher $(-\alpha_i)^2$, requiring a higher $p_{i,j}^y$ to achieve lower point-wise abstain loss, which is desirable for inliers. Likewise, higher α_i penalties are allocated to outlier samples to minimize point-wise penalty loss. This leads to lower $(-\alpha_i)^2$, requiring a lower $\{p_{i,j}^y \mid j = 1, \dots, c\}$ to achieve lower point-wise abstain loss.

As such, the total loss can be expressed as follows:

$$\ell^{\text{total}} := \lambda^{\text{abstain}} \ell^{\text{abstain}} + \lambda^{\text{penalty}} \ell^{\text{penalty}} \quad (10)$$

Anomaly Synthesis Pipeline

REAL synthesizes anomaly by resizing the objects presenting in existing scene, as depicted in the upper panel of Fig. 1-(b). However, we observe that this synthesis pipeline fails to adequately represent real anomaly in two aspects: 1) the limited variety of objects in the existing scene makes it challenging to compensate for the lack of semantically rich features through resizing; 2) learning from these synthesized anomalies may lead to a model that classifies real anomaly solely based on point sparsity. As such, we resort to an additional dataset, ShapeNet (Chang et al. 2015), which consists

of 220,000 models classified into 3,135 categories, to design our new synthesis pipeline.

Specifically, as shown in Fig. 4, we randomly select and **load** $G \sim \text{Binomial}(20, 0.3)$ objects from ShapeNet into the given scene \mathbf{x} , where the probability of not adding any object into \mathbf{x} is also considered. The $\text{Binomial}(a, b)$ generates a random value from a binomial distribution with ‘a’ trials and ‘b’ probability of success per trial.

For each object $s \in \mathbb{R}^{l \times 3}$, we first **rotate** it into its upright pose. Then, we **move** s away from x^c , which is the center of the scene \mathbf{x} , along the x-axis by $d^x \sim \text{Uniform}(r^{\min}, 0.8 * r^{\max})$ that r^{\min} is the distance of the closest point from x^c and r^{\max} is the furthest point from x^c . The $\text{Uniform}(a, b)$ generates a random value from a uniform distribution with lower bound ‘a’ and upper bound ‘b’. Then, we **rotate** s around x^c on the xy-plane for $d^{\text{lon}} \sim \text{Uniform}(0, 360)$ degrees and denote the resulting object as $s = (\mathbf{u}, \mathbf{v}, \mathbf{w})$.

There is a probability that s does not overlap with \mathbf{x} , after moving and rotating. Therefore, if s is positioned outside of \mathbf{x} , the subsequent merge operation is not carried out. Specifically, we stop synthesis process if:

$$\min \{ |\bar{u} - i| + |\bar{v} - j| \} > \Delta, (i, j, k) \in \mathbf{x} \quad (11)$$

Here, \bar{u} and \bar{v} represent the mean u and mean v of s , respectively. We set Δ to 1 in our experiments.

Afterward, since the objects from ShapeNet tend to be smaller in size compared to those in the existing scene, we proceed to **resize** s by a factor of $k \sim \text{Uniform}(1, 7)$. Following this, we **put s on ground**: $\tilde{\mathbf{w}} = \mathbf{w} - \Delta_w$, where Δ_w represents the distance between the bottom of s ($\min \mathbf{w}$) and the point on \mathbf{x} that are the closest to s when looking from the above. The resulting object is $s = (\mathbf{u}, \mathbf{v}, \tilde{\mathbf{w}})$.

Note that terminating the synthesis process at the ‘put on ground’ stage is an alternative design. However, this may lead to trivial solutions in anomaly detection, similar to the issue encountered in REAL, namely, relying on the property of point sparsity for anomaly detection. Hence, we merge s into \mathbf{x} by adjusting the radii of \mathbf{x} , which enables s to adhere to the realistic LiDAR distribution. Specifically, we first represent s and \mathbf{x} using spherical coordinates, resulting in:

$$\mathbf{s} := \{s_j = (\text{lon}_j, \text{lat}_j, r_j) \mid j = 1, \dots, l\} \quad (12)$$

$$\mathbf{x} := \{x_k = (\text{lon}_k, \text{lat}_k, r_k) \mid k = 1, \dots, n\}$$

Here, the lon represents longitude, lat represents latitude, and r represents radius. For each x_k , we replace r_k with r_j if s_j satisfy $|\text{lon}_k - \text{lon}_j| < \Delta_{\text{lon}}$ and $|\text{lat}_k - \text{lat}_j| < \Delta_{\text{lat}}$. During our experiment, we set Δ_{lon} to 0.02 and Δ_{lat} to 0.2. When multiple s_j satisfy the above criterion, we use their smallest r to replace r_k .

Dynamic penalty to further capture the differences between samples. As shown in Fig. 1-(b), the object synthesized through resizing is greater ‘weirdness’ in terms of point sparsity when compared to the ShapeNet object.

Table 2: Comparisons with previous methods. C3D refers to the base segmentation model, Cylinder3D (Zhu et al. 2021).

Method	Semantic Kitti (Behley et al. 2019)			NuScenes (Caesar et al. 2020)		
	AUPR	AUROC	mIoU _{old}	AUPR	AUROC	mIoU _{old}
Closed-set C3D	-	-	58.00	-	-	58.70
C3D + MSP (Hendrycks and Gimpel 2018)	6.70	74.00	58.00	4.30	76.70	58.70
C3D + MaxLogit (Hendrycks et al. 2019)	7.60	70.50	58.00	8.30	79.40	58.70
C3D + MC-Dropout (Gal and Ghahramani 2016)	7.40	74.70	58.00	14.90	82.60	58.70
C3D + REAL (Cen et al. 2022)	20.08	84.90	57.80 (0.20 ↓)	21.20	84.50	56.80
C3D + APF (Li and Dong 2023)	36.10	85.60	57.30 (0.70 ↓)	-	-	-
C3D + P ² AD (ours)	44.68 (8.58 ↑)	92.69 (7.09 ↑)	57.56 (0.44 ↓)	31.58 (10.38 ↑)	95.24 (10.74 ↑)	59.11 (0.41 ↑)

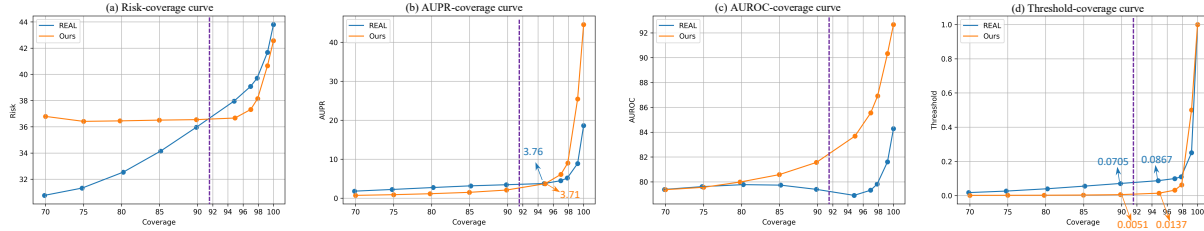


Figure 6: Comparison with the SOTA using the Risk/AUPR/AUROC/Threshold-Coverage curves.

Hence, to maximize the benefits of the point-wise training paradigm, we introduce a point-wise dynamic penalty loss to handle different samples in a customized manner:

$$\ell^{\text{dynamic penalty}} :=$$

$$\frac{1}{m} \sum_{S_m} \frac{1}{n} \sum_{i=1}^n \left\{ \mathbb{I}(y_i \neq c+1 \& y_i \neq c+2) \max(\alpha_i - \beta_{\text{in}} m_{\text{in}}, 0) \right. \\ \left. + \mathbb{I}(y_i = c+1) \max(\beta_{\text{rout}} m_{\text{rout}} - \alpha_i, 0) \right. \\ \left. + \mathbb{I}(y_i = c+2) \max(\beta_{\text{sout}} m_{\text{sout}} - \alpha_i, 0) \right\} \quad (13)$$

The $\{c+2\}$ denotes the outlier class label generated by ShapeNet. The weight parameter β associated with the threshold m is initialized as 1 and is learnable. In our experimental setting, we set the value of m_{sout} to -7, and m_{rout} to -6. Consequently, the total loss becomes:

$$\ell^{\text{total}} := \lambda^{\text{abstain}} \ell^{\text{abstain}} + \lambda^{\text{dynamic penalty}} \ell^{\text{dynamic penalty}} \quad (14)$$

Experiments

Dataset

SemanticKITTI (Behley et al. 2019) is a large-scale driving-scene dataset designed for point cloud segmentation. The dataset is derived from the KITTI Vision Odometry Benchmark and point cloud are collected using the Velodyne-HDLE64 LiDAR in Germany. The dataset consists of 22 sequences, with sequences 00 to 10 utilized as the training set, where sequence 08 serves as the validation set, and sequences 11 to 21 used as the test set. After merging classes with different moving statuses and ignoring classes with a small number of points, 19 classes remain for training and evaluation. Consistent with prior work (Cen et al. 2022), we designate $\{\text{other-vehicle}\}$ as outlier class.

NuScenes (Caesar et al. 2020) consists of 1000 scenes, each lasting 20 seconds, captured using a 32-

beam LiDAR sensor. It contains 40,000 frames sampled at 20Hz and has official training and validation splits. After merging similar classes and removing rare classes, there are 16 remaining classes for training and evaluation. The classes designated as outliers include barrier, constructive-vehicle, traffic-cone, trailer.

Evaluation Metric

Separate evaluation metrics. Consistent with previous work (Cen et al. 2022), we employ inlier mean intersection over union (mIoU_{old}) metric to evaluate the performance of inlier classification, while the AUPR and AUROC are utilized to assess the performance of outlier classification.

Joint evaluation metrics. In this work, due to the lack of intuitiveness of $\hat{r} \in \mathbb{R}^+$, We propose an alternative risk measure by considering the complement of the mIoU_{old}:

$$\hat{r}(f, g|S_m) := \frac{100 - \text{mIoU}_{\text{old}}^{S_m|g}}{\phi(g|S_m)} \quad (15)$$

Here, $\text{mIoU}_{\text{old}}^{S_m|g}$ represents the mIoU_{old} calculated for the sub-dataset S_m under the selective model condition g . Thus, the $\hat{r} \in [0, 100]$ provides a more intuitive understanding.

Comparisons with State-of-the-art Methods

To ensure a fair comparison, we utilize Cylinder3D (Zhu et al. 2021) as the baseline segmentation model.

Quantitative comparison: As illustrated in Tab. 2, our method achieves a new SOTA in anomalous class segmentation for SemanticKITTI and NuScenes, surpassing the previous SOTA by a significant margin. Specifically, our method achieves an AUPR of 44.68 and an AUROC of 92.69, which exceeded the previous SOTA scores of 8.58 and 7.09 in SemanticKITTI. Moreover, our method achieves an AUPR of 31.58 and an AUROC of 95.24 in NuScenes, which exceeded the previous SOTA scores of 10.38 and 10.74, respectively. However, our method exhibits a degradation of 0.24 in the inlier classification performance, which is lower than the previous method APF (Li and Dong 2023).

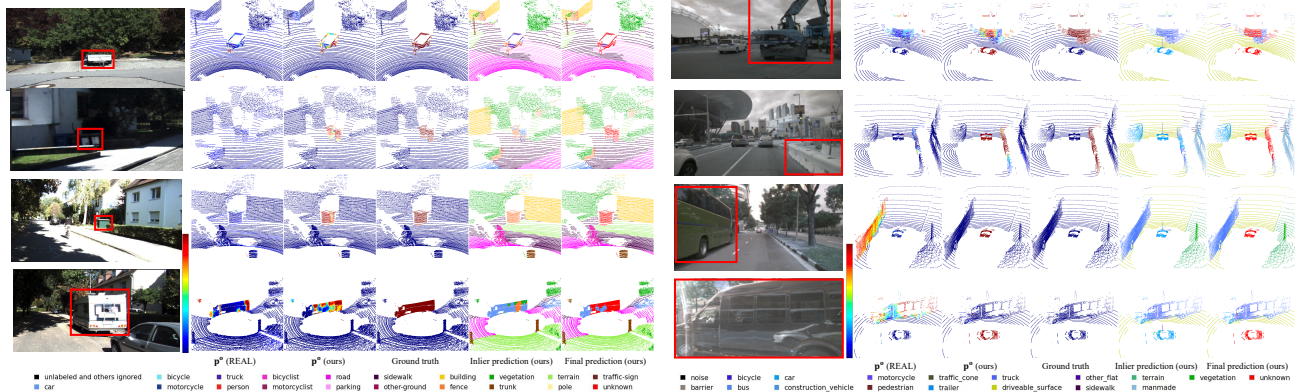


Figure 7: Qualitative comparison results for SemanticKITTI (left) and NuScenes (right); Inlier prediction indicates semantic segmentation; The final prediction is obtained by integrating the inlier prediction with p^o using a threshold of 0.5.

Nonetheless, we believe that this degradation is trivial compared to the substantial improvement we have achieved in the outlier classification.

Qualitative comparison: Consistent with our quantitative results, the qualitative results, as shown in Fig. 7, demonstrate higher response values in real outlier areas compared to REAL. These findings provide further evidence of the superiority of our point-wise abstaining penalty training paradigm. Since the code for APF is still unavailable, we could not compare our method with it.

Risk-Coverage curve comparison: As shown in Fig. 6-(a), our method achieves a lower risk than REAL when full coverage is applied. With decreasing coverage, both our method and REAL show reduced risk.

Why our method achieve a higher risk compared to REAL when coverage is below 90? (purple dotted line)

There are several reasons behind this phenomenon. Firstly, the threshold for coverage below 90 is close to 0, as shown in Fig. 6-(d). This indicates that our method is confident about all the remaining samples, making it challenging to reject any samples. In such cases, there is a high probability of rejecting true positive samples, which adversely affects the performance. Secondly, as illustrated in Fig. 6-(b) and -(c), the AUPR is 3.711, while the AUROC is approximately 80. These results suggest a significant imbalance between true negative and true positive samples, with the latter often being hard samples with low p^o . This imbalance leads to worse risk as the coverage becomes lower than 90.

However, we firmly believe that robust performance in high coverage is more critical than in low coverage since anomalous objects are extremely rare in the real world. Low coverage is characterized by a large number of samples in the perceived scene being classified as anomaly, which is not feasible in real-world applications.

Ablation Study

Effectiveness of dynamic abstaining penalty. As demonstrated in Tab. 3, the penalty setting is denoted by Equ. 10, while the dynamic penalty setting is represented by Equ. 14. The dynamic penalty setting achieved the best performance. These results provide evidence for the effectiveness of our

Table 3: Ablations for dynamic penalty setting in SemanticKITTI.

Penalty	Dynamic Penalty	AUPR	AUROC	mIoU _{old}
✓	✓	43.69 44.68	92.51 92.69	57.47 57.56

Table 4: Ablation study on pseudo outlier sample synthesis pipeline in SemanticKITTI.

ShapeNet-based	resizing-based	AUPR	AUROC	mIoU _{old}
✓	✓	29.14 (14.55 ↓) 41.82 (1.87 ↓)	89.56 (2.95 ↓) 93.04 (0.53 ↑)	57.31 (0.16 ↓) 57.30 (0.17 ↓)
✓	✓	43.69	92.51	57.47

dynamic penalty supervising signal design.

Effectiveness of anomaly synthesis pipeline. We conduct an ablation study of anomaly synthesis pipeline. The results, as presented in Tab. 4, demonstrate a decrease in AUPR by 1.87 and an increase in AUROC by 0.53, when the ShapeNet-based anomaly synthesis pipeline is not utilized. Notably, the AUPR and AUROC values drop significantly by 14.55 and 2.95, respectively, without the resizing-based anomaly synthesis pipeline. This raises the question of **whether ShapeNet-based synthesis pipeline is trivial**.

To address this concern, we conduct an ablation study of anomaly synthesis pipeline by plotting the risk-coverage curve. As shown in Fig. 5-(right), the blue line (resizing-based) shows an initial decrease in risk followed by an increase. This phenomenon can be further explained as the rejection of true predictions of the inlier samples, resulting in a deterioration of the inlier classification.

On the other hand, the ShapeNet-based synthesis pipeline (orange line) exhibits a consistent reduction in risk as the coverage decreases. This phenomenon can be attributed to the rejection of outlier or misclassified samples. Hence, the ShapeNet-based synthesis pipeline can synthesize objects that are more similar to real anomaly, including those that are prone to misclassification.

Finally, by combining these two synthesis pipeline, our method achieves the best performance with low risk at high coverage and a stable decrease in risk as coverage decreases.

Conclusion

In this work, we first revisit previous methods using the unified theoretical framework of selective classification and propose our new formulation which effectively captures the subtle differences between known and anomalous samples. Furthermore, we design a novel anomaly synthesis pipeline that leverages the richness of the ShapeNet dataset and adheres to the realistic LiDAR distribution to compensate for the lack of semantically rich features. Experimental results demonstrate the superiority of our method across both traditional anomaly detection metrics and newly introduced metrics associated with selective classification. Our method has achieved SOTA performance on public benchmark datasets.

References

- Behley, J.; Garbade, M.; Milioto, A.; Quenzel, J.; Behnke, S.; Stachniss, C.; and Gall, J. 2019. Semantickitti: A dataset for semantic scene understanding of lidar sequences. In *Proceedings of the IEEE/CVF international conference on computer vision*, 9297–9307.
- Bevandić, P.; Krešo, I.; Oršić, M.; and Šegvić, S. 2021. Dense outlier detection and open-set recognition based on training with noisy negative images. *arXiv preprint arXiv:2101.09193*.
- Caesar, H.; Bankiti, V.; Lang, A. H.; Vora, S.; Liong, V. E.; Xu, Q.; Krishnan, A.; Pan, Y.; Baldan, G.; and Beijbom, O. 2020. nuscenes: A multimodal dataset for autonomous driving. In *Proceedings of the IEEE/CVF conference on computer vision and pattern recognition*, 11621–11631.
- Cen, J.; Yun, P.; Zhang, S.; Cai, J.; Luan, D.; Tang, M.; Liu, M.; and Yu Wang, M. 2022. Open-world semantic segmentation for lidar point clouds. In *Computer Vision—ECCV 2022: 17th European Conference, Tel Aviv, Israel, October 23–27, 2022, Proceedings, Part XXXVIII*, 318–334. Springer.
- Chan, R.; Rottmann, M.; and Gottschalk, H. 2021. Entropy maximization and meta classification for out-of-distribution detection in semantic segmentation. In *Proceedings of the IEEE/CVF international conference on computer vision*, 5128–5137.
- Chang, A. X.; Funkhouser, T.; Guibas, L.; Hanrahan, P.; Huang, Q.; Li, Z.; Savarese, S.; Savva, M.; Song, S.; Su, H.; et al. 2015. Shapenet: An information-rich 3d model repository. *arXiv preprint arXiv:1512.03012*.
- Charoenphakdee, N.; Cui, Z.; Zhang, Y.; and Sugiyama, M. 2021. Classification with rejection based on cost-sensitive classification. In *International Conference on Machine Learning*, 1507–1517. PMLR.
- Chow, C. 1970. On optimum recognition error and reject tradeoff. *IEEE Transactions on information theory*, 16(1): 41–46.
- Cordts, M.; Omran, M.; Ramos, S.; Rehfeld, T.; Enzweiler, M.; Benenson, R.; Franke, U.; Roth, S.; and Schiele, B. 2016. The cityscapes dataset for semantic urban scene understanding. In *Proceedings of the IEEE conference on computer vision and pattern recognition*, 3213–3223.
- El-Yaniv, R.; et al. 2010. On the Foundations of Noise-free Selective Classification. *Journal of Machine Learning Research*, 11(5).
- Feng, L.; Ahmed, M. O.; Hajimirsadeghi, H.; and Abdi, A. H. 2023. Towards Better Selective Classification. In *The Eleventh International Conference on Learning Representations*.
- Gal, Y.; and Ghahramani, Z. 2016. Dropout as a bayesian approximation: Representing model uncertainty in deep learning. In *international conference on machine learning*, 1050–1059. PMLR.
- Geifman, Y.; and El-Yaniv, R. 2017. Selective classification for deep neural networks. *Advances in neural information processing systems*, 30.
- Geifman, Y.; and El-Yaniv, R. 2019. Selectivenet: A deep neural network with an integrated reject option. In *International conference on machine learning*, 2151–2159. PMLR.
- Grcić, M.; Bevandić, P.; and Šegvić, S. 2022. Densehybrid: Hybrid anomaly detection for dense open-set recognition. In *European Conference on Computer Vision*, 500–517. Springer.
- Handa, A.; Patraucean, V.; Badrinarayanan, V.; Stent, S.; and Cipolla, R. 2016. Understanding real world indoor scenes with synthetic data. In *Proceedings of the IEEE conference on computer vision and pattern recognition*, 4077–4085.
- Hendrycks, D.; Basart, S.; Mazeika, M.; Zou, A.; Kwon, J.; Mostajabi, M.; Steinhardt, J.; and Song, D. 2019. Scaling out-of-distribution detection for real-world settings. *arXiv preprint arXiv:1911.11132*.
- Hendrycks, D.; and Gimpel, K. 2018. A Baseline for Detecting Misclassified and Out-of-Distribution Examples in Neural Networks. In *ICLR 2017*. arXiv.
- Hendrycks, D.; Mazeika, M.; and Dietterich, T. 2018. Deep anomaly detection with outlier exposure. *arXiv preprint arXiv:1812.04606*.
- Jung, S.; Lee, J.; Gwak, D.; Choi, S.; and Choo, J. 2021. Standardized max logits: A simple yet effective approach for identifying unexpected road obstacles in urban-scene segmentation. In *Proceedings of the IEEE/CVF International Conference on Computer Vision*, 15425–15434.
- Li, J.; and Dong, Q. 2023. Open-Set Semantic Segmentation for Point Clouds via Adversarial Prototype Framework. In *Proceedings of the IEEE/CVF Conference on Computer Vision and Pattern Recognition*, 9425–9434.
- Lin, T.-Y.; Maire, M.; Belongie, S.; Hays, J.; Perona, P.; Ramanan, D.; Dollár, P.; and Zitnick, C. L. 2014. Microsoft coco: Common objects in context. In *Computer Vision—ECCV 2014: 13th European Conference, Zurich, Switzerland, September 6-12, 2014, Proceedings, Part V 13*, 740–755. Springer.
- Liu, Y.; Ding, C.; Tian, Y.; Pang, G.; Belagiannis, V.; Reid, I.; and Carneiro, G. 2022. Residual Pattern Learning for Pixel-wise Out-of-Distribution Detection in Semantic Segmentation. *arxiv:2211.14512*.

- Liu, Z.; Wang, Z.; Liang, P. P.; Salakhutdinov, R. R.; Morency, L.-P.; and Ueda, M. 2019. Deep gamblers: Learning to abstain with portfolio theory. *Advances in Neural Information Processing Systems*, 32.
- McCormac, J.; Handa, A.; Leutenegger, S.; and Davison, A. J. 2017. Scenenet rgb-d: Can 5m synthetic images beat generic imagenet pre-training on indoor segmentation? In *Proceedings of the IEEE International Conference on Computer Vision*, 2678–2687.
- Movshovitz-Attias, Y.; Kanade, T.; and Sheikh, Y. 2016. How Useful Is Photo-Realistic Rendering for Visual Learning? In *ECCV*. arXiv.
- Mozannar, H.; and Sontag, D. 2020. Consistent Estimators for Learning to Defer to an Expert. In *ICML2020*.
- Song, S.; Yu, F.; Zeng, A.; Chang, A. X.; Savva, M.; and Funkhouser, T. 2017. Semantic scene completion from a single depth image. In *Proceedings of the IEEE conference on computer vision and pattern recognition*, 1746–1754.
- Su, H.; Qi, C. R.; Li, Y.; and Guibas, L. J. 2015. Render for CNN: Viewpoint Estimation in Images Using CNNs Trained with Rendered 3D Model Views. In *2015 IEEE International Conference on Computer Vision (ICCV)*, 2686–2694. Santiago, Chile: IEEE. ISBN 978-1-4673-8391-2.
- Tian, B.; Liu, M.; Gao, H.-a.; Li, P.; Zhao, H.; and Zhou, G. 2023. Unsupervised Road Anomaly Detection with Language Anchors. In *2023 IEEE International Conference on Robotics and Automation (ICRA)*, 7778–7785. IEEE.
- Tian, Y.; Liu, Y.; Pang, G.; Liu, F.; Chen, Y.; and Carneiro, G. 2022. Pixel-wise energy-biased abstention learning for anomaly segmentation on complex urban driving scenes. In *Computer Vision—ECCV 2022: 17th European Conference, Tel Aviv, Israel, October 23–27, 2022, Proceedings, Part XXXIX*, 246–263. Springer.
- Zhang, Y.; Bai, M.; Kohli, P.; Izadi, S.; and Xiao, J. 2017a. Deepcontext: Context-encoding neural pathways for 3d holistic scene understanding. In *Proceedings of the IEEE international conference on computer vision*, 1192–1201.
- Zhang, Y.; Song, S.; Yumer, E.; Savva, M.; Lee, J.-Y.; Jin, H.; and Funkhouser, T. 2017b. Physically-Based Rendering for Indoor Scene Understanding Using Convolutional Neural Networks. In *2017 IEEE Conference on Computer Vision and Pattern Recognition (CVPR)*, 5057–5065. Honolulu, HI: IEEE. ISBN 978-1-5386-0457-1.
- Zhu, X.; Zhou, H.; Wang, T.; Hong, F.; Ma, Y.; Li, W.; Li, H.; and Lin, D. 2021. Cylindrical and asymmetrical 3d convolution networks for lidar segmentation. In *Proceedings of the IEEE/CVF conference on computer vision and pattern recognition*, 9939–9948.